Avalanche Photodiodes With Dual Multiplication Layers and Ultra-High Responsivity-Bandwidth Products for FMCW Lidar System Applications

Zohauddin Ahmad, Sheng-I Kuo, You-Chia Chang, Rui-Lin Chao, None Naseem, Yi-Shan Lee, Yung-Jr Hung, *Member, IEEE*, Huang-Ming Chen, Jason Chen, Chee Seong Goh, and Jin-Wei Shi, *Senior Member, IEEE*

(Invited Paper)

***Abstract*—In this work, we demonstrate a novel $In_{0.52}Al_{0.48}As$ based top-illuminated avalanche photodiode (APD), designed to circumvent the problem of serious bandwidth degradation under high gain (>100) and high power operation and significantly enhance the dynamic range in the established frequency modulated continuous wave (FMCW) lidar system. In our APD design, the carriers transiting through the dual multiplication (M-)layers are subjected to a stepped-up electric field profile, so they can be energized by the first step and propagate to the second step to trigger the avalanche processes. Such a cascade avalanche process leads to an ultra-high gain bandwidth product (460 GHz) with a 1 A/W responsivity at unit gain. Compared to the high-performance and commercial p-i-n PD and photo-receiver (PD + trans-impedance amplifier (TIA)) installed in the same lidar test bed, our demonstrated APD receiver (without TIA) has a larger S/N ratio under high operation gain (33 A/W) with less optical local-oscillator (LO) power required (0.25 vs. 0.5 mW), while exhibiting a wider dynamic range in each pixel. These advantages in turn lead to the construction of a better quality of 3-D lidar image by using the demonstrated APD.**

***Index Terms*—Avalanche photodiode, p-i-n photodiode.**

Manuscript received October 30, 2020; revised January 14, 2021; accepted February 22, 2021. Date of publication March 3, 2021; date of current version August 17, 2021. This work was supported by the Ministry of Science and Technology in Taiwan under Grants 108-2622-E-008-011 -CC2, 107-2622-E-008 -002 -CC2, and 106-2221-E-008 -063 -MY3. *(Corresponding author: Jin-Wei Shi.)*

Zohauddin Ahmad, None Naseem, Yi-Shan Lee, and Jin-Wei Shi are with the Department of Electrical Engineering, National Central University, Taoyuan 320, Taiwan (e-mail: zohauddin145991@st.jmi.ac.in; naseemever3@gmail.com; queenalee@ee.ncu.edu.tw; jwshi@ee.ncu.edu.tw).

Sheng-I Kuo, You-Chia Chang, Huang-Ming Chen, and Jason Chen are with the Department of Photonics and Institute of Electro-Optical Engineering, National Chiao Tung University, Hsinchu 300, Taiwan (e-mail: shengi.eo08g@nctu.edu.tw; youchia@nctu.edu.tw; pchen@nctu.edu.tw; jchen@mail.nctu.edu.tw).

Rui-Lin Chao is with the Department of Electrical Engineering, National Central University, Taoyuan 320, Taiwan, and also with the Department of Photonics and Institute of Electro-Optical Engineering, National Chiao Tung University, Hsinchu 300, Taiwan (e-mail: obscurotation.eo03g@g2.nctu.edu.tw).

Yung-Jr Hung is with the Department of Photonics, National Sun Yat-sen University, Kaohsiung 804, Taiwan (e-mail: yungjr@mail.nsysu.edu.tw).

Chee Seong Goh is with the Alnair Labs Corporation, Tokyo 141-0031, Japan (e-mail: goh@alnair-labs.com).

Color versions of one or more figures in this article are available at https://doi.org/10.1109/JSTQE.2021.3062637.

Digital Object Identifier 10.1109/JSTQE.2021.3062637

I. Introduction

THE development of light detection and ranging (lidar) technologies has continued unabated and has found many applications in autonomous cars, robots, medical applications and unmanned aerial vehicles [1]–[3]. In contrast to the pulsed time-of-flight (ToF) lidar system operating around the 905 nm wavelength regime, a frequency-modulated continuous-wave (FMCW) lidar system which can be operated at telecommunication wavelengths (∼1550 nm) is attractive because it can leverage the advanced technology of the well-developed fiber communication industry and achieve excellent resolution without requiring any fast electronics or high peak optical power [4]–[10]. Furthermore, the interference issues in ToF systems, which can be attributed to the multiple reflected optical pulses from different objects, can be eliminated.

In these two kinds of lidar systems, two different receiver end schemes are adopted to handle the weak reflected light. The ToF system usually adopts single-photon APDs operated at Geiger mode with infinite gain for direct-detection (D-D) [11]. With respect to FMCW lidar, the high-linearity p-i-n photodiode (PD) integrated with the self-heterodyne beating detecting setup is usually preferred for serving as its receiver-end. The weak received light can be amplified by strong optical local-oscillator (LO) power pumping onto the PD [12]. Nevertheless, in the advanced photonic integrated circuit (PIC) based FMCW lidar system, significant optical insertion loss remains a challenge, which leads to a limited output optical LO power (several mWs) [9], [10], [13], [14]. In order to compensate for such on-chip insertion loss, a semiconductor optical amplifier (SOA), which is monolithically integrated with the high-power waveguide type uni-traveling carrier photodiodes (UTC-PDs) has been successfully demonstrated [15], [16] for application in a coherent communication system. However, for lidar applications, the size of the optical aperture of the waveguide type PD is usually too small to capture the weak light reflected from the object. Vertically-illuminated type APDs with a large aperture size, high responsivity, and high internal gain (around 20 dB), which is comparable with SOA, as well as low excess noise, and decent performance of speed under moderate (∼mW)

optical LO pumping powers, are highly desired for modern chip-scale or PIC based lidar applications. However, for most of the reported InP or $In_{0.52}Al_{0.48}As$ based APDs, there is usually serious degradation in their speed and excess noise performance with the increase of avalanche gain. In order to overcome the problematic trade-off between avalanche gain and excess noise, the $In_{0.52}Al_{0.48}As$ based tandem APD structure has been demonstrated to effectively reduce the excess noise of APD under high-gain operation [17], [18]. State-of-the-art sensitivity has been demonstrated for 1.25 Gbit/sec data communication [18]. However, compared with that of traditional APDs, its gain-bandwidth product (GBP) performance is sacrificed for low excess noise performance due to the slowdown of the hole avalanche process in its multiplication layer [17].

In this work, we demonstrate a novel $In_{0.52}Al_{0.48}A$ based vertically-illuminated APD. By use of a novel design of dual multiplication (M-) layers, the trade-off between avalanche gain and bandwidth can be greatly relaxed. An ultra-high gain bandwidth product (460 GHz) and high responsivity (1 A/W) at unit gain can be achieved by using a device with a large optical window diameter (200 μm). We use such an APD connected with a RF low-noise-amplifier (LNA) to serve as the receiver-end in our home-made FMCW lidar system. The optimum bias voltage for the highest quality of captured lidar image is achieved with a responsivity as high as 33 A/W and a 1.25 GHz 3-dB bandwidth. Compared to the commercially available p-i-n PD and p-i-n PD based photo-receiver, our demonstrated APD receiver can have a larger S/N ratio under high operation gain (33 A/W), with a lower required optical local-oscillator (LO) power (0.25 vs. 0.5 mW), while exhibiting a wider dynamic range in each pixel. These advantages in turn lead to a better quality of constructed 3-D lidar image.

II. Design of Device Structure and Fabrication

Fig. 1(a) shows a conceptual cross-sectional view of the demonstrated APDs with a top view in the inset. Fig. 1(b) shows the band diagram of the demonstrated APDs along the AA' axis. Note that Fig. 1(a) is not drawn in scale. From top to bottom, the structure of our devices is composed of a p^+-$In_{0.53}Ga_{0.47}As$ contact layer, p^+-$In_{0.52}Al_{0.48}As$ window layer, intrinsic $In_{0.53}Ga_{0.47}As$ absorbing layer, two p-type $In_{0.52}Al_{0.48}As$ charge layers, and two intrinsic $In_{0.52}Al_{0.48}As$ multiplication layers and N^+ $In_{0.52}Al_{0.48}As$ /InP contact layers. Two $In_{0.52}Al_xGa_{0.48-x}As$ graded bandgap layers are inserted in the interfaces between the absorber/window and absorber/multiplication layers, respectively. The thickness of each epi-layer is specified in detail in this figure. As can be seen, the 500 nm thick multiplication (M-) layer is divided into two partitions of 200 nm and 300 nm by an additional charge control layer to obtain a stepped electric field profile [19], [20]. The electric field distribution within the device is simulated by using the Silvaco Technology Computer Aided Design (TCAD) tools.[1] Fig. 2(a) shows the calculated electric fields of the demonstrated

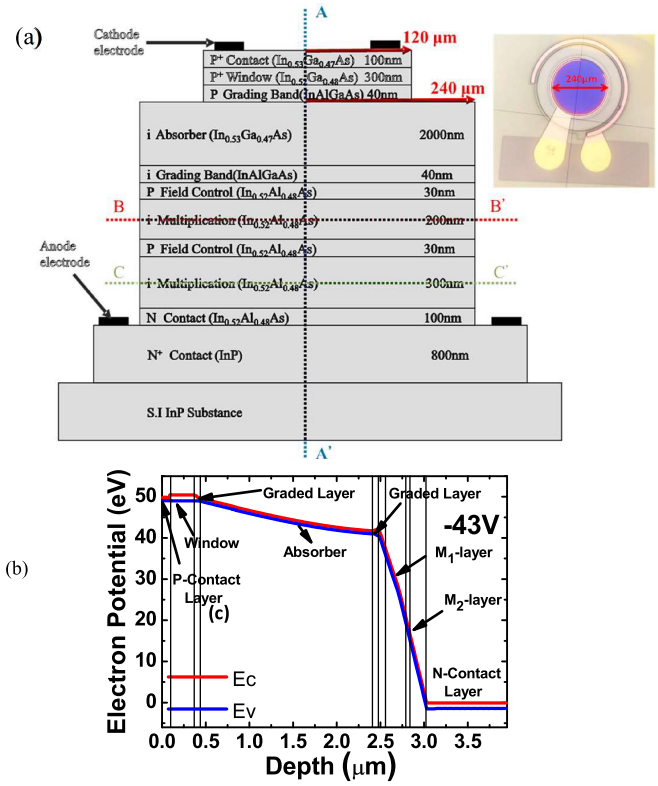

Fig. 1. (a) Conceptual cross-sectional view of the demonstrated APD. The radius of the active mesa is 120 μm, as specified in this figure. Inset shows the top view. (b) Simulated band diagram of the fabricated device along AA'.

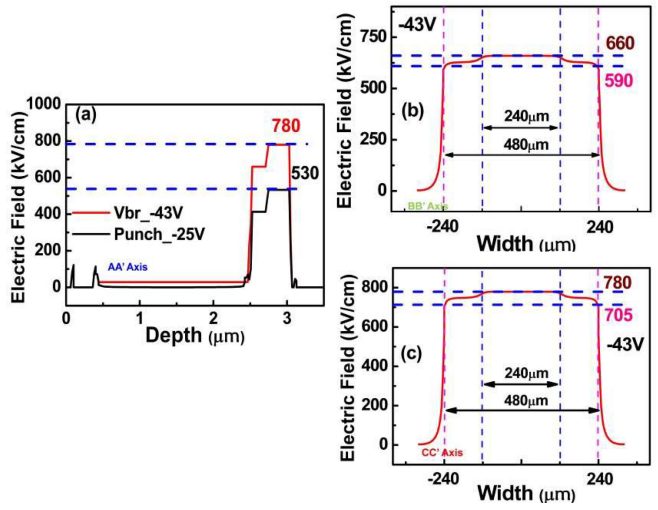

Fig. 2. (a) Electric field profiles at V_{pt} and V_{br} along the vertical direction AA'. Electric field profiles at V_{br} for the (b) first and (c) second (bottom) multiplication layer along lateral directions BB' and CC', respectively.

APD along the vertical direction (AA') at the punch-through (V_{pt}) and breakdown voltage (V_{br}).

Due to the stepped electric (E-) field profile, the electrons will be energized by the first M-layer with a thickness of 200 nm, where the electric field strength is not high enough to trigger significant impact ionization, and then transit to the second 300 nm thick M-layer to initiate successive impact ionization. This

[1]Silvaco, 2811 Mission College Boulevard, 6th floor, Santa Clara, CA 95054.

design provides better localization of impact ionization than can be achieved in a uniformly thick 500 nm M-layer, which can reduce the delay time induced by the avalanche process in the APD. The use of a stepped E-field may also reduce excess noise (k-factor) in the APD. In our demonstrated device structure, the hole impact ionizations are suppressed because of the lower E-field encountered as they travel back toward the absorption layer. Furthermore, the cascade avalanche process in the demonstrated dual M-layer structure avoids pushing the single M-layer into the deep avalanche regime under the desired high-gain operation. Overall, a shorter avalanche delay time, a lower excess noise (k-) factor, and a larger GBP than those obtained with the traditional APD design with the same M-layer thickness can thus be expected for our dual M-layer design. In our previous work [20], using dual $In_{0.52}Al_{0.48}As$ M-layers with different thicknesses of 60 and 90 nm, the APD exhibited bandwidth-responsivity product ($\sim$180 GHz $\times$ A/W) and k-factor ($\sim$0.14) values close to those of the high-performance $In_{0.52}Al_{0.48}As$ APD with the traditional single M-layer design and with a thickness of only 90 nm [21]. This result suggests that our dual M-layer design offers superior performance in terms of noise and GBP to that of the conventional APD design with the single M-layer and the same M-layer thickness. Similar working principles are realized for the impact-ionization-engineered (I_2E) APD structures [22], [23] which localizes the impact ionization process in the materials with the narrowest bandgap in the M-layer, which is hetero-junction with several different bandgap materials. In contrast to the I_2E structure, our M-layer acts as a homo-junction but with several charge layers and different doping densities to localize the avalanche process in the region which has the highest E-field.

As shown in Fig. 1(a), the triple mesa structure is adopted to confine the E-field in the first mesa (active region) with a diameter of 240 μm, which is etched through the p-type window layer and stops at the 2 μm thick $In_{0.53}Ga_{0.47}As$ absorption layer [24]. Figs 2(b) and (c) show the calculated electric fields for the demonstrated APD along horizontal directions (BB' and CC'), respectively, at the first and second M-layers under a breakdown voltage of (-43 V), which will be discussed later. We can clearly see, as expected, that there is a discrepancy in the M-layer electric (E-) field between the active region (first mesa) and the edge of the mesa. Better confinement of the E-field to suppress edge breakdown in the proposed APD structure can be realized by the etching of an inverted n-side up structure [21] or mesa structure through the charge layer [19], [20]. However, edge breakdown may not be a serious issue in our demonstrated APD due to the large active diameter (240 μm) of the first mesa. The inset to Fig. 1(a) shows a top-view of the device fabricated with a 240 μm diameter active mesa. The diameter of the active optical window is 200 μm. Such a large window diameter is beneficial for the collection of weak reflected light in our established lidar system, which will be discussed in detail later.

III. Device Measurement Results

Figs 3 shows the measured bias-dependent dark current, photocurrent, and operation gain of the demonstrated APDs, subject to different optical pumping powers at an optical wavelength of

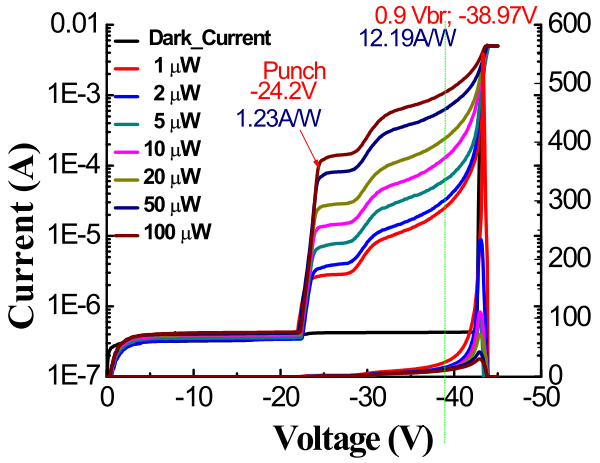

Fig. 3. The measured dark current, photocurrent, and operation gain versus bias voltages under different optical pumping powers of the demonstrated APD at the 1.55 μm wavelength. The specified values of responsivity are measured under 50 μW.

1.55 μm. As can be seen, the measured breakdown voltage (V_{br}) and punch through voltage (V_{pt}) are around -43 and -24.2 V, respectively.

We assume a zero coupling loss and single-pass of injected light into the absorption layer of our device. With a 2 μm-thick $In_{0.53}Ga_{0.47}As$ absorption layer, the theoretical maximum unit gain responsivity will be around 1 A/W at the 1.55 μm wavelength. Here, the photo-absorption constant used for the $In_{0.53}Ga_{0.47}As$ layer at such a wavelength is around 0.8 μm^{-1} [25]. The gain versus bias voltages under different optical pumping powers (1 to 100 μW) are also provided in the figures for reference. As can be seen, there is a significant reduction in all the measured operation gains when the reverse bias voltage is over V_{br} due to the tremendous increase of dark current, which occupies most of the measured total current (i.e., summation of photocurrent and dark current). In addition, we can clearly see that the maximum operation gain gradually decreases with increasing pumping power. This phenomenon can be explained by the space charge screening (SCS) effect induced by the photo-generated holes in the thick and undoped $In_{0.53}Ga_{0.47}As$ absorption layer, which reduces the net E-field and multiplication gain in the M-layer [20].

Figs 4 and 5 show the bias-dependent O-E frequency responses measured under a low (1 μW) and high (100 and 240 μW) optical pumping power at the 1.55 μm wavelength, respectively. Under such a low optical pumping power, we can clearly see that the measured 3-dB O-E bandwidths can be sustained at the same value ($\sim$1.25 GHz) with an increase of the reverse bias voltage (operation gain). Only a slight degradation on bandwidth (from 1.25 to 0.95 GHz) can be observed under the -43 V bias, which is close to V_{br}. This is in contrast to the phenomenon reported for most APDs, which usually exhibit a significant degradation in the O-E bandwidth with an increase in the operation gain due to the increase in the avalanche induced delay time with the gain. The trade-off between operation gain and speed can be fundamentally overcome because of the cascade avalanche processes in our dual M-layer design, as discussed above. On the other hand, as shown in Fig. 5, the

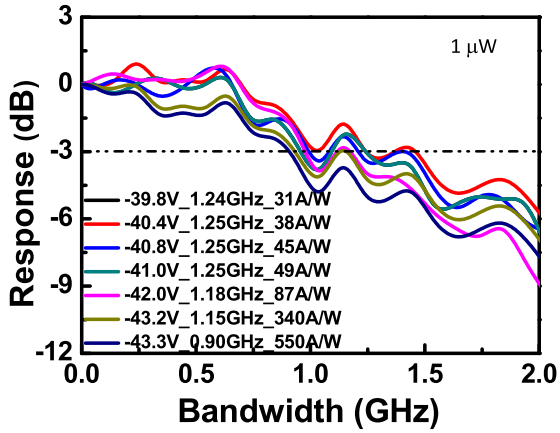

Fig. 4. The measured bias dependent O-E frequency responses of the demonstrated APD under a 1 μW optical pumping power at the 1.55 μ m wavelength.

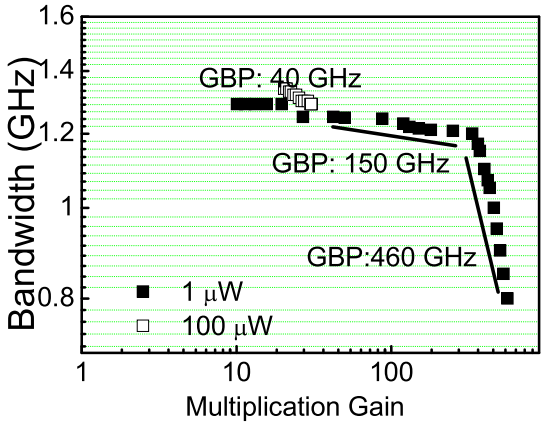

Fig. 6. The measured 3-dB O-E bandwidths versus multiplication gain of the demonstrated APD at low (1 μW) and high (0.1 mW) optical pumping powers.

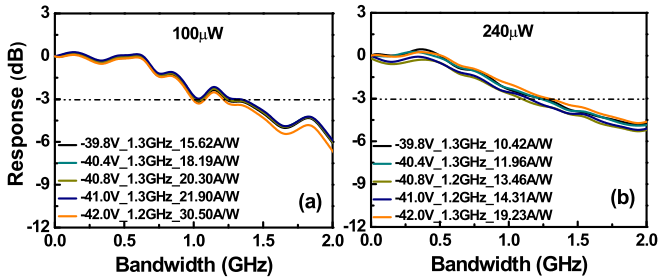

Fig. 5. The measured bias dependent O-E frequency responses of the demonstrated APD under a 100 and 240 μW optical pumping power at the 1.55 μ m wavelength.

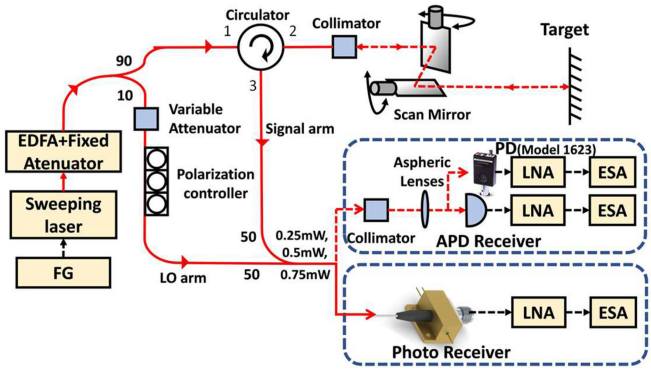

Fig. 7. Conceptual diagram of the demonstrated FMCW lidar system. Three different kinds of Rx are adopted in our system for comparison. FG: function generator. EDFA: erbium-doped fiber amplifier. LNA: low-noise amplifier. ESA: electrical spectrum analyzer. Red solid line: optical path in fiber. Red dash line: optical path in free space.

measured 3-dB O-E bandwidths are pinned at around 1.3 GHz, regardless of the changes in the reverse bias voltages. These bandwidth values are close to the maximum O-E bandwidths of the device measured under low power excitation, as shown in Fig. 4. Such invariant high-speed performance can be attributed to the values of the operation gain significantly decreasing and becoming much less sensitive to the reverse bias voltage under high-power operation, as shown in Fig. 3. The delay time induced by the avalanched gain, which is the major bandwidth limiting factor of an APD under high-gain (high-bias) operation is thus minimized, resulting in the observed invariant 3-dB O-E bandwidth [20].

Fig. 6 shows the 3-dB O-E bandwidths versus operation gains of the demonstrated APD measured under low (1 μW) and high (100 μW) optical pumping powers. As can be seen, for the low pumping power case, our demonstrated device can achieve a gain-bandwidth (GB) product as high as 460 GHz with a 1 A/W unit-gain external responsivity. On the other hand, there is a gradual decrease in the values of the GB product when the optical pumping power reaches 100 μW, which can be attributed to the reduction in the multiplication gain versus the increase of optical power [20]. The achieved high GB product (460 GHz) can be attributed to the cascade avalanche process in the dual M-layers, as discussed earlier. Furthermore, compared to the gain-bandwidth curves of typical APDs, which usually exhibit monotonic decreases of bandwidth with the increase of the multiplication gain [21], [26], our device curves exhibit different trends. As can be seen, our demonstrated APD has a good operation window, which means a constant O-E bandwidth ($\sim$1.25 GHz) can be sustained over a wide range of operation gains (from 10 to $\sim$300). This should be of great benefit in applications for FMCW lidar, which will be discussed in detail later.

IV. FMCW LIDAR SYSTEMS

We built an FMCW lidar system with a fiber-based self-heterodyne interferometer and mechanical scanning mirrors [27], as shown in Fig. 7. The laser source is split into a signal path and a local-oscillator (LO) path using a 90/10 fiber splitter. The signal light passes through a circulator and a fiber collimator, producing a beam with a spot size of 0.87 mm ($1/e^2$ diameter) and a full-angle divergence angle of 0.129°. We use two scanning galvanometer mirrors to steer the beam in two dimensions with a field of view of $\pm$12.5° and a mechanical repeatability of 15 μrad (Thorlabs GVSM002-US). The received light is redirected by the circulator to follow a different path and then combined with the LO via a 50/50 fiber splitter. A variable attenuator is included in the LO path for power adjustment. The combined signal and LO light is fed to the receiver (Rx) part of the demonstrated lidar

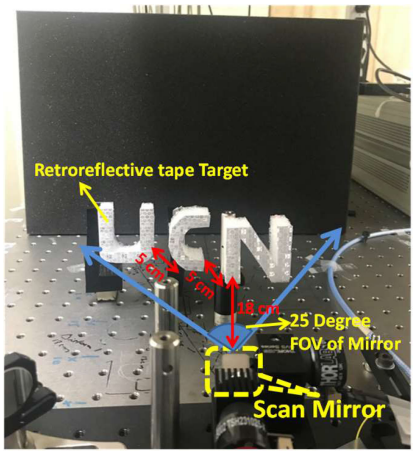

Fig. 8. Picture of the demonstrated FMCW lidar with N, C, and U targets as OUTs for testing. FOV: field of view.

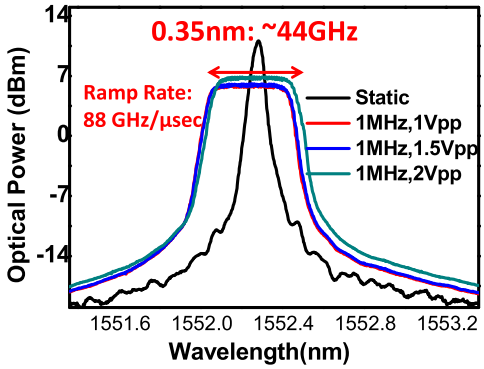

Fig. 9. The measured optical spectra of our wavelength sweeping laser under different driving-voltages (V_{pp}).

system. Three kinds of Rx are adopted and their performance compared in detail. One is our demonstrated APD as discussed above and the second one is the commercially available p-i-n PDs based Rx (PT-40D/8XLMD)[2], which is composed of a high-speed p-i-n PD integrated with a trans-impedance amplifier (TIA). This module has a fiber pigtail package which can provide a 35 GHz bandwidth and 1300 V/W conversion gain. The final p-i-n PD module integrated with a 50 Ω load (Newport 1623)[3] has an $In_{0.53}Ga_{0.47}As$ photo-absorption layer. This PD module has a ball lens in its optical window to collect the free-space input light. It is powered by a battery for low-noise performance and has a responsivity of 1 A/W with a 3-dB O-E bandwidth at around 0.6 GHz. All kinds of Rx (APD, p-i-n PD, and p-i-n PD + TIA) are then connected with the same low-noise amplifier (LNA; Miteq AM-1309)[4] to further boost the magnitude of the O-E converted signal. The photomixing down-converted IF signal output from the PD module or APD is then sent into an RF spectrum analyzer for analysis. A collimator followed by an aspherical lens is adopted in our setup to feed the combined optical LO with reflected signals from the object to the window of our home-made APD chip, without an optics package, and the commercial p-i-n PD module. It forms a spot size of 23 μm ($1/e^2$ diameter). The lidar system is tested using targets made from Styrofoam shaped like the letters N, C, and U. The targets were covered with retroreflective tapes and place at certain distances, as shown in Fig. 8.

Aside from the receiver, the transmitter side also plays an important role in the FMCW lidar system. Wavelength sweeping can be realized by changing the bias current to the mirrors of tunable sampled grating distributed Bragg reflector (SGDBR) lasers [10], usually integrated with an external feedback loop to linearize the wavelength sweeping process [10]. However, the loop bandwidth usually limits the maximum ramp rate for wavelength sweeping. The other approach for wavelength sweeping is through the use of the linewidth enhancement effect (LEE) in distributed-feedback lasers (DFB) [28] or single-mode VCSELs [6]. By pushing these lasers into the saturation regime and driving them with large current pulses, a significant frequency modulation (FM) with a suppressed amplitude modulation (AM) can be achieved due to LEE. However, the residual amplitude modulation (RAM) noise and nonlinear relation of wavelength shift versus driving current both remain challenges [8]. Here, the working principle of our sweeping laser is based on the LEE. A conceptual diagram of its function blocks appears in our previous works [29], [30]. This module fully customized design by Alnair Labs[5] is primarily composed of a commercially available distributed feedback (DFB) laser chip (NEL Laser Diodes; NLK1C6DAAA),[6] alternating current (AC) laser current driving circuit, and an optical limiting amplifier [31]. Compared with the sweeping laser reported in our previous work [29], [30], we obtain a further increase in the maximum wavelength ramp rate from 10.3 to 88 GHz/μs by improving the laser driving circuit. During wavelength sweeping operation, the driving circuit is used to convert and amplify the external injected voltage signal into current waveforms to effectively modulate the output optical amplitude of the DFB laser. Due to the LEE (chirp parameter) in this DFB laser [32], the values of the central wavelength can also be swept with the variation of output optical power (injected carrier density). In order to obtain a strong LEE (FM), it is necessary to use huge amplitude current pulses (hundreds of mA) to modulate our DFB laser chip. An optical limiting amplifier is integrated with the output of the DFB laser chip to minimize serious RAM during wavelength sweeping. Fig. 9 shows the output optical spectra of our sweeping laser measured under 1 MHz sweeping rate and different driving voltages. The central wavelength of a sweeping laser under static operation (no AC driving signal injection) is also shown here for reference. The measured 3-dB linewidth (0.06 nm; 7.5 GHz) is much broader than the specification of the adopted DFB laser (∼100 KHz) and this can be attributed to the limited resolution (∼0.05 nm) of our optical spectrum analyzer (Ando AQ6315A). As can be seen, the scanning wavelength range will slightly enhance with an increase in the amplitude of the driving voltage and flat topped output optical spectra can be realized. This result implies that the

[2]Picometrix, LLC. 2925 Boardwalk, Ann Arbor, MI, 48014.
[3]Newport Corporation, 1791 Deere Avenue, Irvine, CA, 92606.
[4]L3Harris Narda-MITEQ, 435 Moreland Road, Hauppauge, NY, 11788.
[5]Alnair Labs Corporation, Westside Gotanda 2F, 6-2-7 Nishi-Gotanda, Shinagawa-ku, Tokyo 141-0031, Japan.
[6]NTT Electronics, New Stage YOKOHAMA, 1-1-32 Shin-urashimacho, Kanagawa-ku, Yokohama-shi, Kanagawa, 221-0031, Japan.

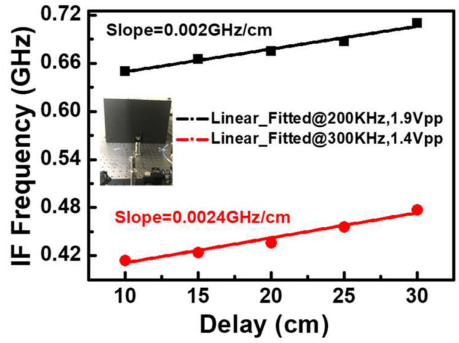

Fig. 10. The IF beating frequency versus different delay line distances for two different driving conditions (200 KHz; 1.9 V_{pp} and 300 kHz; 1.4 V_{pp}) on the sweeping laser. The inset shows a picture of the measurement setup.

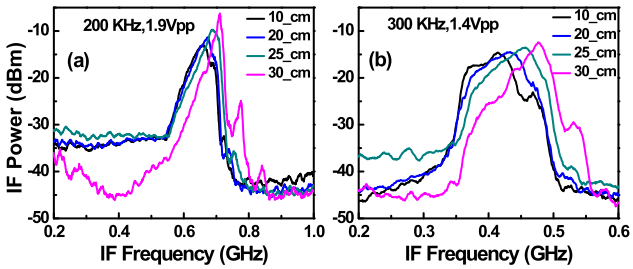

Fig. 11. The measured IF spectra for different delay line distances for modulation frequencies of (a) 200 KHz and (b) 300 KHz on the wavelength sweeping laser.

RAM noise during FM modulation has been well suppressed in our sweeping laser output and its wavelength ramp rate is nearly 1000 times faster than that of the reported DFB with an external feedback loop (88 GHz/μs vs. 100 GHz/ms) [28]. Here the ramp rate is determined by both the sweeping (modulation) frequency and amplitude of the driving voltage (V_{pp}).

V. FMCW Lidar Measurement Results

Fig. 10 shows the self-heterodyne beating intermediate frequency (IF) versus different delay line distances (time) under two different driving conditions, which are specified on the figures, for our sweeping laser source. For measurement, the metal plate (reflector) served as the object under test (OUT); the setup is shown in the inset to Fig. 10. The delay line length is achieved by changing the distance between the OUT and the scanning mirror. The IF frequency in an FMCW lidar system is determined by taking the product of the frequency ramp rate and delay time. As can be seen, a linear relation between delay time (distance) and beating frequency can be obtained, which is essential for a high-performance FMCW lidar system. The distance information can be determined according to the slope of these traces and the measured IF frequency of the OUT, which will be discussed in detail later. Fig. 11 shows the corresponding output IF spectra from the commercial photoreceiver (p-i-n PD + TIA). In order to compare the performances of different Rxs in the established FMCW lidar systems, we measured the signal-to-noise ratio (SNR) of the down-converted IF signal output from the three Rxs based on the above setup. Fig. 12 shows the measured SNR versus received optical power of the

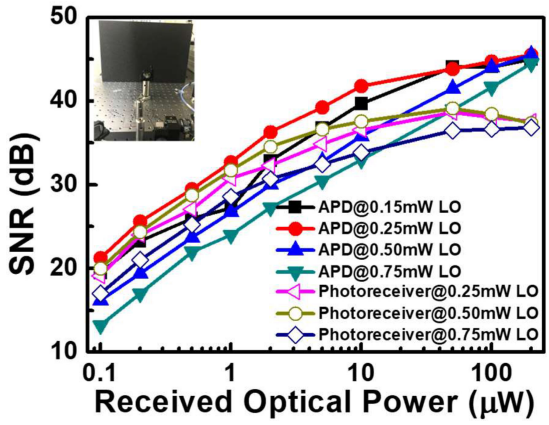

Fig. 12. The measured SNR vs. received optical power under different optical LO pumping powers onto APDs and photoreceiver (p-i-n PD + TIA). The APD bias is fixed at −40 V.

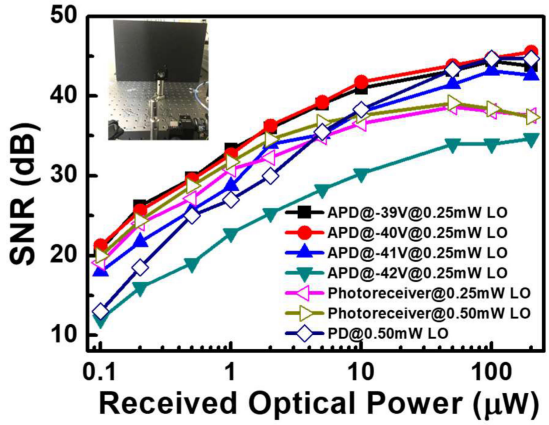

Fig. 13. The measured SNR vs. received optical power of APDs (under different reverse bias voltages), photoreceiver (p-i-n PD + TIA), and p-i-n PD. The optical LO pumping powers on the p-i-n PD and APD are 0.5 and 0.25 mW, respectively.

photoreceiver (p-i-n PDs + TIA) and APDs under a fixed reverse dc bias at −40 V. Here, the SNR is defined by the difference in power levels between the peak of the IF tone and the noise floor. The received optical power represents the measured optical power in the 3rd port of the circulator, as shown in Fig. 7. In the measurement, we vary the optical LO pumping power on the two receivers to find out their optimized operating conditions. As can be seen, the optimized optical LO power for the highest SNR of the APD and photoreceiver is 0.25 and 0.5 mW, respectively. Furthermore, our APD based receiver has a better SNR than that of the p-i-n + TIA module, over the whole range of received optical powers (0.1 to 200 μW), with a lower required optical LO power.

In addition to the optical LO pumping power, the applied bias voltage onto the APD also has a deterministic effect on the system's SNR. Fig. 13 shows the measured SNR versus received optical power of the commercial p-i-n PDs, commercial photoreceiver (p-i-n PD + TIA), and APDs under different reverse bias voltages. Figs 14 (a) and (b) show the corresponding IF spectra for the APD and photoreceiver (p-i-n + TIA), respectively, under the whole range of received optical power. Here, according to the

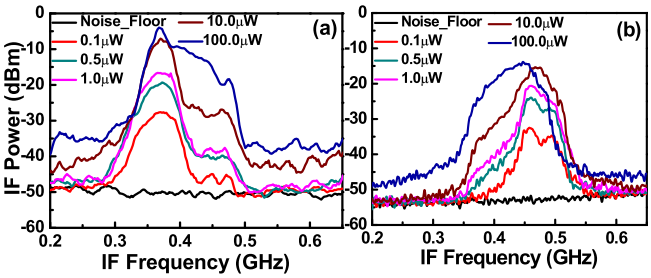

Fig. 14. The measured IF spectra for the cases of different received optical power for (a) APD under −40 V bias and 0.25 mW LO power and (b) p-i-n PD + TIA under 0.5 mW LO power.

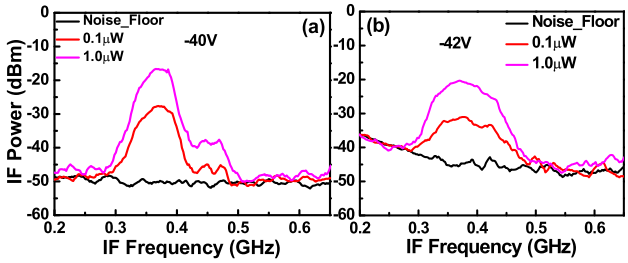

Fig. 15. The measured IF spectra for the cases of different received optical powers for an (a) APD under −40 V bias and 0.25 mW LO power and (b) APD under −42 V and 0.25 mW LO power.

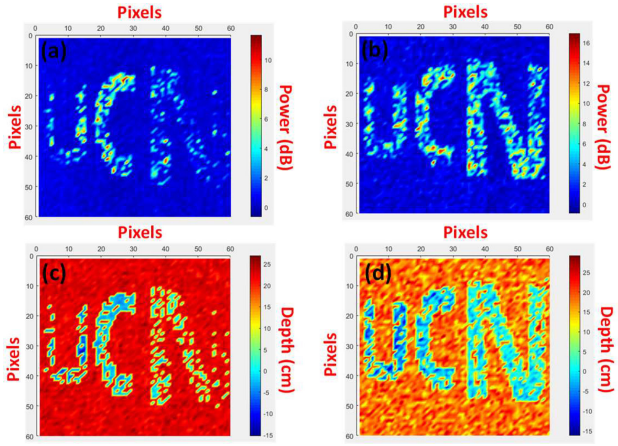

Fig. 16. The captured lidar images based on the measured IF power of each pixel from the (a) p-i-n PD + TIA and (b) APD. The captured lidar images based on the measured IF frequency of each pixel from the (c) p-i-n PD + TIA and (d) APD.

measurement results shown in Fig. 12, the launched optical LO power to the p-i-n and APD based receiver is 0.5 and 0.25 mW, respectively, needed in order to obtain the optimized SNRs. As can be seen, under a −40 V bias on the APD, the measured SNR of the APD is around 10 dB larger than that of the commercial p-i-n PD (no TIA) under low received optical power (0.1 μW). Besides, the measured SNR of our APD is also slightly better ($\sim$1 dB) than that of high-performance photoreceiver (p-i-n PD+TIA) under such low received power. This can be attributed to the fact that the multiplication gain ($\sim$1650 V/W) of the APD is even larger than the trans-impedance gain provided by the TIA ($\sim$1300 V/W). Here, the conversion gain of the APD module is obtained by assuming a 50 Ω load integrated with the APD output and its responsivity (33 A/W) under a −40 V bias.

On the other hand, when the received optical power becomes larger (>5 μW), both our home-made APD and commercial p-i-n PD exhibit significant better SNR than that of photoreceiver (PD+TIA). This result can be attributed to the excellent high-power performance of our home-made APD chip. Under heterodyne beating measurement, our APD device (without LNA integration) exhibits a saturation current over 12 mA under 0.9 V_{br} operation. The overload optical power of the photoreceiver is only +3 dBm, which corresponds to an output photocurrent of around 1.2 mA. This saturation current which is much smaller than that of our homemade APD (1.2 vs. 12 mA), can be attributed to the much smaller photo-absorption volume in the p-i-n PD for its wider O-E bandwidth (35 vs. 1.2 GHz) performance and the maximum allowable output current from its integrated TIA. Obtaining such a high saturation current for our APD can be understood as follows: In contrast to the behaviors of a typical p-i-n PD under high optical power illumination, the degradation in the O-E bandwidth and saturation of the photo-generated RF power from the APDs is minimized due to the gain reduction effect [20]. As illustrated in Fig. 5, even for a launched optical power on the APD as high as 0.24 mW, there is no significant O-E bandwidth degradation.

As shown in Fig. 3, by further increasing the reverse bias voltage on the APD, a higher responsivity and SNR can be expected. Fig. 15 shows the measured IF spectra of our APD under different optical receiving power and reverse bias voltages. As can be seen, although the responsivity is greatly enhanced when the bias shifts from −40 to −42 V, this is accompanied by an increase in the noise floor rather than contributing to the signal power.

Fig. 16 shows images of the OUTs (N, C, and U) captured by using the photoreceiver (p-i-n PD + TIA) and APD based Rx. These images are constructed based on the down-converted IF frequencies and power in each pixel. The setups for such measurements are shown in Figs 7 and 8. Here, the output optical power from the scanning mirror is around 15 mW and the captured optical power reflected from the OUTs is around several μWs. The wavelength sweeping laser is modulated at a 200 KHz ac signal with a 1.9 V_{pp} (peak-to-peak driving voltage). The values of the optical LO pumping power and bias voltages applied to the APDs and photoreceiver have been optimized according to the measurement results, as shown in Figs 12 to 15. From Figs 16 (a) and (b), we can clearly see that the images of the letter N captured using the APD based Rx have a larger contrast ratio in IF power and better quality of image than those of the p-i-n PD based photoreceiver. This result confirms that the APD has a superior SNR to that of the photoreceiver when the received optical power becomes larger, as shown in Figs 12 and 13, and the letter N has the strongest reflected optical signal among the three letters because it is closest to the light emission aperture of the lidar. By using the slopes of the IF frequency vs. delay distance as illustrated in Fig. 10 and the difference in IF frequency between the pixels of the targets, we can directly obtain the depth information about these objects. Here we choose the averaged values of the measured IF frequency from each pixels of letter N as our reference frequency. Figs 16 (c) and

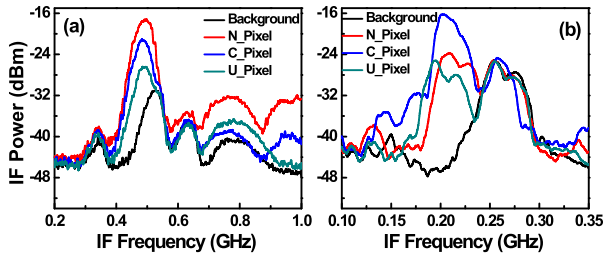

Fig. 17. The captured IF spectra of a single pixel from the background and the N, C and U shaped targets obtained using the (a) APD and (b) p-i-n PD + TIA.

(d) show the images with depth information obtained using the p-i-n + TIA and APD based Rx, respectively. We can clearly see that letter "N" locates at reference plane as discussed and the lidar measured distances between "C" and "U" is around 5 and 10 cm, respectively. These values match very well with the real distances between these three targets, as shown in Fig. 8. Fig. 17 shows the typical measured IF spectra of pixels from the targets (N, C, and U) and the backgrounds. Here, the background signal is induced by the parasitic reflections between the port 3 of circulator and the coupling optics (collimators or fiber connectors) for feeding the light onto Rx. Obviously, APD the based Rx can provide a narrower linewidth of IF signal, which leads to clearer depth information than that of the p-i-n based device, as shown in Fig. 16. Besides, there is a difference in frequency of the IF beating signal obtained from the APD and photoreceiver (p-i-n + TIA) based Rx ($\sim$0.53 vs. $\sim$0.25 GHz) under the same driving condition (200 KHz; 1.9 V_{pp}) of the wavelength sweeping laser. It can be attributed to the combined optical signals (LO with signal arms) must pass through the dispersive fiber and then feed into the photoreceiver with the fiber pigtail package. The dispersion in fiber thus changes the relative phases between these two optical arms and induce the variation in frequency of beating signal.

VI. Conclusion

In conclusion, we demonstrate novel top-illuminated APD structures with excellent performance for FMCW lidar applications. By making use of dual M-layer designs with a cascade avalanche process, such APDs can fundamentally relax the trade-off between the multiplication gain and the speed. Under low power excitation ($\sim$1 μW), such a device with a high unit gain responsivity (1 A/W) can maintain an invariable speed performance ($\sim$1.2 GHz) over a wide range of operation gains (10 to 300). In order to verify the excellent performance of our demonstrated APD for lidar applications, we constructed an FMCW lidar system based on the 2-D scanning mirror and a sweeping laser source. As compared to the commercially available p-i-n PD based Rx (PD+TIA and PD), the APD based device, which has no additional integration with TIA, can provide a larger SNR, with less required optical LO power (0.25 vs. 0.5 mW), a wider dynamic range over a broad range of received optical powers (0.1 to 200 μW) in each pixel, and a high operation gain ($\sim$33 A/W; $-$40 V). The superior performance of the APD to p-i-n PD in turn leads a better quality of 3-D lidar images.

References

[1] J.-W. Shi, J.-I. Guo, M. Kagami, P. Suni, and O. Ziemann, "Photonic technologies for autonomous cars: Feature introduction," *Opt. Exp.*, vol. 27, pp. 7627–7628, 2019.
[2] [Online]. Available: http://www.woodsidecap.com/wp-content/uploads/2018/04/Yole_WCP-LiDAR-Report_April-2018-FINAL.pdf
[3] J. Hecht, "Lidar for self-driving cars," *Opt. Photon. News,* vol. 29, no. 1, pp. 26–33, Jan. 2018.
[4] B. Behroozpour *et al.*, "Chip-scale electro-optical 3D FMCW lidar with 8 μm ranging precision," *ISSCC Dig. Tech. Papers*, San Francisco, CA, USA, pp. 214–215, Feb. 2016.
[5] C. V. Poulton *et al.*, "Coherent solid-state LIDAR with silicon photonic optical phased arrays," *Opt. Lett.*, vol. 42, no. 20, pp. 4091–4094, Oct. 2017.
[6] T. Hariyama, P. A. M. Sandborn, M. Watanabe, and M. C. Wu, "High-accuracy range-sensing system based on FMCW using low-cost VCSEL," *Opt. Exp.,* vol. 26, no. 7, pp. 9285–9297, Apr. 2018.
[7] S. Crouch, "Advantages of 3D imaging coherent lidar for autonomous driving applications," in *Proc. 19th Coherent Laser Radar Conf.*, pp. 1–4, Jun. 2018.
[8] X. Zhang, J. Pouls, and M. Wu, "Laser frequency sweep linearization by iterative learning pre-distortion for FMCW LiDAR," *Opt. Exp.*, vol. 27, no. 7, pp. 9965–9974, Apr. 2019.
[9] A. Martin *et al.*, "Photonic integrated circuit-based FMCW coherent LiDAR," *J. Lightw. Technol.*, vol. 36, pp. 4640–4645, Oct. 2018.
[10] B. J. Isaac, B. Song, S. Pinna, L. A. Coldren, and J. Klamkin, "Indium phosphide photonic integrated circuit transceiver for FMCW LiDAR," *IEEE J. Sel. Topics Quantum Electron.*, vol. 25, no. 6, Nov./Dec. 2019, Art. no. 8000107.
[11] B. F. Aull *et al.*, "Large-format Geiger-mode avalanche photodiode arrays and readout circuits," *IEEE J. Sel. Topics Quantum Electron.,* vol. 24, no. 2, Mar./Apr. 2018, Art. no. 3800510.
[12] P. Adany, C. Allen, and R. Hui, "Chirped lidar using simplified homodyne detection," *IEEE/OSA J. Lightw. Technol.,* vol. 27, no. 16, pp. 3351–3357, Aug. 2009.
[13] W. Xie *et al.*, "Heterogeneous silicon photonics sensing for autonomous cars," *Opt. Exp.,* vol. 27, pp. 3642–3662, Feb. 2019.
[14] Y. Zhang *et al.*, "Sub-wavelength-pitch silicon-photonic optical phased array for large Field-of-Regard coherent optical beam steering," *Opt. Exp.,* vol. 27, pp. 1929–1940, Feb. 2019.
[15] J. W. Raring *et al.*, "40 Gbit/s photonic receivers integrating UTC photodiodes with high- and low-confinement SOAs using quantum well intermixing and MOCVD regrowth," *Electron. Lett.*, vol. 42, no. 16, pp. 942–943, Aug. 2006.
[16] M. Anagnosti *et al.*, "Record gain x bandwidth (6.1 THz) monolithically integrated SOA-UTC photoreceiver for 100-Gbit/s applications," *J. Lightw. Technol.*, vol. 33, no. 6, pp. 1186–1190, Mar. 2015.
[17] W. Sun, X. Zheng, Z. Lu, and J. C. Campbell, "Monte Carlo simulation of InAlAs/InAlGaAs tandem avalanche photodiodes," *IEEE J. Quantum Electron.*, vol. 48, no. 4, pp. 528–532, Apr. 2012.
[18] M. S. Ferraro *et al.*, "Position sensing and high bandwidth data communication using impact ionization engineered APD arrays," *IEEE Photon. Technol. Lett.*, vol. 31, no. 1, pp. 58–61, Jan. 2019.
[19] Y.-H. Chen *et al.*, "Top-illuminated $In_{0.52}Al_{0.48}As$-based avalanche photodiode with dual charge layers for high-speed and low dark current performances," *IEEE J. Sel. Topics Quantum Electron.,* vol. 24, no. 2, Mar./Apr. 2018, Art. no. 3800208.
[20] H.-Y. Zhao *et al.*, "High-speed avalanche photodiodes with wide dynamic range performance," *J. Lightw. Technol.*, vol. 37, no. 23, pp. 5945–5952, Dec. 2019.
[21] M. Nada, Y. Yamada, and H. Matsuzaki, "Responsivity-bandwidth limit of avalanche photodiodes: Toward future ethernet systems," *IEEE J. Sel. Top. Quantum Electron.,* vol. 24, no. 2, Mar./Apr. 2018, Art no. 3800811.
[22] S. Wang *et al.*, "Low-noise avalanche photodiodes with graded impact-ionization-engineered multiplication region," *IEEE Photon. Technol. Lett.*, vol., vol. 13, no. 12, pp. 1346–1348, Dec. 2001.
[23] N. Duan *et al.*, "High-speed and low-noise SACM avalanche photodiodes with an impact-ionization-engineered multiplication region," *IEEE Photon. Technol. Lett.*, vol., vol. 17, no. 8, pp. 1719–1721, Aug. 2005.
[24] B. F. Levine *et al.*, "A new planar InGaAs.InAlAs avalanche photodiode," *IEEE Photon. Tech. Lett.,* vol. 18, no. 18, pp. 1898–1900, Sep. 2006.
[25] Z. A. Naseem *et al.*, "The enhancement in speed and responsivity of uni-traveling carrier photodiodes with $GaAs_{0.5}Sb_{0.5}/In_{0.53}Ga_{0.47}As$ type-II hybrid absorbers," *Opt. Exp.,* vol. 27, no. 11, pp. 15495–15504, May, 2019.
[26] J. C. Campbell *et al.*, "Recent advances in avalanche photodiodes," *IEEE J. Sel. Topics Quantum Electron.,* vol. 10, pp. 777–787, Jul./Aug. 2004.

[27] Z. W. Barber, J. R. Dahl, T. L. Sharpe, and B. I. Erkmen, "Shot noise statistics and information theory of sensitivity limits in frequency-modulated continuous-wave ladar," *J. Opt. Soc. Am. A*, vol. 30, no. 7, Jul. 2013, Art. no. 1335.
[28] N. Satyan, A. Vasilyev, G. Rakuljic, V. Leyva, and A. Yariv, "Precise control of broadband frequency chirps using optoelectronic feedback," *Opt. Exp.,* vol. 17, no. 18, pp. 15991–15999, Aug. 2009.
[29] J.-W. Shi *et al.*, "Photonic generation and wireless transmission of linearly/nonlinearly continuously tunable chirped millimeter-wave waveforms with high time-bandwidth product at W-band," *IEEE Photon. J.,* vol. 4, no. 1, pp. 215–223, Feb. 2012.
[30] J.-M. Wun *et al.*, "Photonic chirped radio-frequency generator with ultrafast sweeping rate and ultra-wide sweeping range," *Opt. Exp.,* vol. 21, no. 9, pp. 11475–11481, May 2013.
[31] O. C. Graydon, M. N. Zervas, and R. I. Laming, "Erbium-doped-fiber optical limiting amplifiers," *J. Lightw. Technol.*, vol. 13, no. 5, pp. 732–739, May 1995.
[32] A. Villafranca, J. A. Lázaro, I. Salinas, and I. Garcés, "Measurement of the linewidth enhancement factor in DFB lasers using a high-resolution optical spectrum analyzer," *IEEE Photon. Technol. Lett.*, vol. 17, no. 11, pp. 2268–2270, Nov. 2005.

Zohauddin Ahmad was born in Bihar, India, in 1989. He graduated from the Department of Nanoscience and Nanotechnology, Jamia Millia Islamia, New Delhi, India. He is currently working toward the Ph.D. degree with the Department of Electrical Engineering, National Central University, Taoyuan City, Taiwan. His current research interests include high-speed modulator-based lasers, FMCW-Lidar, and photonics integrated circuits.

Sheng-I Kuo was born in Taoyuan, Taiwan, on November 12, 1996. He received the B.S. degree from the Department of Physics, National Chung Hsing University, Taichung, Taiwan, in 2019. He is currently working toward the M.S. degree with the Institute of Electro-Optical Engineering, National Chiao Tung University, Hsinchu, Taiwan, under the guidance of Prof. You-Chia Chang.

You-Chia Chang was born in Taichung, Taiwan, on January 7, 1981. He received the Ph.D. degree in applied physics from the University of Michigan, Ann Arbor, MI, USA, in 2016. In 2018, he was an Assistant Professor with the Department of Photonics and the Institute of Electro-Optical Engineering, National Chiao Tung University, Hsinchu, Taiwan. From 2016 to 2018, he was a Postdoctoral Research Scientist with the Department of Electrical Engineering, Columbia University, New York City, NY, USA. He was the recipient of the Jade Mountain (Yushan) Young Scholar Award in 2018. His research interests include silicon photonics, metamaterials, and 2D materials.

Rui-Lin Chao was born in Taipei, Taiwan, on October, 27, 1991. He received the B.S. degree from the Undergraduate Honors Program of Nano Science and Engineering, Chiao Tung University, Hsinchu, Taiwan, in 2014, and is currently working toward the Ph.D. degree from the Department of Elecro-Optics, Chiao Tung University, under the guidance of Prof. Jyehong Chen and Co-Advisor Prof. Jin-Wei Shi, National Central University, Taoyuan City, Taiwan. His research interests include slow light high speed silicon based modulators, high speed photodetectors, and high speed laser development and design.

None Naseem was born in the Punjab, India in 1991. He received the M. Tech. degree from the Department of Nanotechnology, Jamia Millia Islamia, New Delhi, India. He is currently working toward the Ph.D. degree with the Department of Electrical Engineering, National Central University, Taoyuan City, Taiwan. His current research interests include high-speed photodiodes and avalanche photodiodes for optical receivers.

Yi-Shan Lee was born in Kaohsiung, Taiwan on October 31, 1985. She is currently an Assistant Professor with the Department of Electrical Engineering, National Central University, Taoyuan, Taiwan. Her research interests include the cavity quantum electrodynamics, single photon source, entangled photon source, and single photon avalanche diodes. Her recent publications can be found in *Optics Letters*, IEEE PHOTONICS TECHNOLOGY LETTERS. and *Physical Review Letters*.

Yung-Jr Hung (Member, IEEE) received the B.S. and Ph.D. degrees in electrical engineering from the National Taiwan University of Science and Technology, Taipei, Taiwan, in 2005 and 2010, respectively. He joined the Faculty of the Department of Photonics, National Sun Yat-sen University, Kaohsiung, Taiwan, in 2013 as an Assistant Professor and was promoted to an Associate Professor in 2017. He joined the Department of Electrical and Computer Engineering, University of California at Santa Barbara, Santa Barbara, CA, USA, in 2009 and was a Visiting Scholar till 2010. He has authored or coauthored more than 100 technical journal and conference articles. He was the recipient of IEEE Best Young Professional Member Award in 2019 and the MOST Da-You Wu Memorial Award in 2020. His current research focuses on the area of CMOS-compatible optoelectronic devices.

Huang-Ming Chen received the Ph.D. degree in material sciences from University of Rochester, Rochester, NY, USA, in 2003. He joined the Faculty of the Department of Photonic and Institute of Display, National Chiao Tung University, Hsinchu, Taiwan, after his postdoctoral research in 2004. His current research interests include fast switch liquid crystal photonic devices, gas sensors, and ink-jet printing technology for flexible electronics. He is a member of the Society of Information Display, the International Liquid Crystal Society, and the American Chemical Society.

Jason Chen received the B.S. and M.S. degree in electrical engineering from National Taiwan University, Taipei, Taiwan, in 1988 and 1990, respectively and the Ph.D. degree in electrical engineering and computer science from the University of Maryland Baltimore County, Baltimore, MD, USA, in 1998.

He joined JDSU Uniphase Corporation, in 1998 as a Senior Engineer and obtained 15 U.S. patents. He joined the Faculty of National Chiao-Tung University, Hsinchu, Taiwan, 2003, where he is currently a Professor and the chairman of the Department of Photonics. He authored or coauthored more than 100 papers on international journals and conferences and has been invited to give invited talks with numerous technical conferences including the OFC, the Photonic West, and the ECOC. His research interests include hybrid access network, long reach passive optical networks, and optical interconnects.

Chee Seong Goh was born in Penang, Malaysia on February 23, 1974. In 2000, he received the M.S. degree from the University of Malaya, Kuala Lumpur, Malaysia and the Ph.D. degree from the University of Tokyo, Tokyo, Japan under the Japanese Monbukagakusho Scholarship Program in 2004. He has authored and coauthored more than 30 papers in international journals and conferences in the area of his research interests. His research interests include tunable FBG devices for WDM systems, CNT-based passively mode-locked femtosecond fiber lasers, and high-speed optical sampling systems. He is currently the Chief Executive Officerwith Alnair Labs Corporation, Tokyo, a company that designs, manufactures and markets optical testers and instruments.

Jin-Wei Shi (Sernior Member, IEEE) was born in Kaohsiung, Taiwan on January 22, 1976. In 2003, he joined the Department of Electrical Engineering, National Central University, Taoyuan City, Taiwan, where, since 2011, he has been a Professor. he joined the Electronics and Communication Engineering Department, University of California, Santa Barbara,Santa Barbara, CA, USA, and from 2011 to 2012 and from 2016 to 2017 he was a Visiting Professor. He has authored or coauthored more than four book chapters, 150 journal papers, 200 conference papers, and holds 30 patents. His current research interests include ultra-high speed or power photodetectors, electro-absorption modulators, THz photonic transmitters, and VCSELs In 2010, he was the recipient of the Da-You Wu Memorial Award.